Proceedings World Geothermal Congress 2020+1
Reykjavik, Iceland, April - October 2021

MEQ ~ Permeability –

Haskell Modelling of High Frequency Emissions from Stimulation Microseismicity in the Ambient Crust

Peter Leary & Peter Malin
Advanced Seismic Instrument & Research, 317 E. Millbrook, Raleigh, NC 27609 USA

Keywords: MEQ, microseismicity, seismic sources, spatial correlation, permeability, stimulation, fractures, fluid flow

ABSTRACT

Microseismic activity in magnitude range $-1 < m < 2$ induced by controlled injection of fluid into ambient crystalline rock at 6km depth and recorded by a wellbore sensor array at 2.5km depth above the injection volume shows that the radiated seismic waves are dominated by high frequencies 200 Hz < f < 800 Hz. The observed velocity waveform spectra to not conform to the standard slip-plane phenomenology, e.g., $v(f) \sim v_0 f/(1 + f/f_0)^2$) with characteristic frequency $f_0 \sim 1/L$ scaling inversely with slip surface dimension $L \sim 10^{-m/2}$. We further observe that the statistics of microseismic event spatial correlation and lognormal size distribution are congruent with the statistical distributions of crustal permeability given by $\kappa(x,y,z) \sim \exp(\alpha\varphi(x,y,z))$ for normally-distributed spatially-correlated formation porosity distributions $\varphi(x,y,z)$ with parameter α fixed by the empirical condition $\alpha\underline{\varphi} \sim 3\text{-}5$ for formation mean porosity $\underline{\varphi}$. In the absence of waveform evidence for seismic slip activity on planar surfaces, we use Haskell's formalism for elastodynamic waveform radiation by arbitrary slip dislocation structures to model the observed high frequency waveforms and their spectra. Satisfactory generic waveform attributes proceed from Haskell seismic dislocation fronts moving at low rupture speeds across spatially complex localised distributions $\kappa(x,y,z)$ consistent with crustal permeability empirics. The same computation performed for rapid rupture speeds on planar surfaces gives standard fault-like slip waveform spectra. Our modelling indicates that induced seismicity in ambient crust occurs largely on pre-existing crustal permeability structures of limited physical extent rather than on planar slip surfaces of potentially unlimited physical extent. In these circumstances is logical to expect there is essentially no hazard of run-away earth ruptures occurring during fluid injection in the ambient crust. It is further logical to expect that wellbore fluid pressurization does not induce controllable extensive stress-aligned planar flow structures as commonly speculated in the past.

1. INTRODUCTION

The 1940-60s Gutenberg-Richter (G-R) empiric $N(m) \sim 10^{-bm}$ relates earthquake frequency $N(m)$ to earthquake magnitude m for ongoing and potentially hazardous seismic slip events occurring in major active crustal tectonic fault systems [1-12]. Over the same period of time, expressions for seismic radiation waveforms emitted by major fault-zone earthquakes were derived from the elastodynamics of dislocation slip along planar surfaces [13-17]. Seismic displacement waveforms u(t) were related to the length L, width W and dislocation slip amplitude D for earthquake dislocation events of magnitude $m \sim \log_{10}(LWD)$, and their spectra were found to take elementary forms such as $u(f) \sim u_0/(1 + (f/f_0)^2)$, in which u_0, the net source displacement recorded at the sensor site, is proportional to the product of fault surface area and dislocation LWD, and the characteristic waveform frequency f_0 scales inversely with characteristic fault dimension, $f_0 \sim 1/L$. This seismic radiation waveform analysis was routinely validated over three decades of fault scale length, 0.1km < L < 100km, corresponding to slip event magnitude range $\sim 2 < m < \sim 8$ [18-22].

Following these signal advances, a large literature accumulated in which the seismic slip mechanics of active fault zones for events with $m > \sim 2$ and L > ~100m were applied to crustal microseismic events having $m < \sim 2$ and L < ~100m [e.g., 23-30]. The fault-zone derived G-R power-law scaling exponent b for microseismicity has been extensively treated as a diagnostic parameter for locally induced seismic activity [e.g., 31-41], with reservoir fluid displacement commonly ascribed to cubic-law flow along planar fault surfaces [e.g., 42-59]. It is notable, however, that over the years there has been little progress towards acquiring a systematic view of fault-fault or fault-fluid interactions that can be convincingly related to other crustal or reservoir properties. There is, for instance, no agreed physical reasoning leading to the long-standing G-R fractal relation $N(\ell) \sim N_0(\ell_0/\ell)^d$ expressed for a characteristic event slip surface dimension ℓ [12]. Nor are there established procedures for translating crustal reservoir microseismicity data into a means of identifying where to drill steam production wells in convective geothermal reservoirs [60-61]. As a third example, there remains little instruction from microseismicity data on how to stimulate flow between wellbore pairs for commercial heat extraction from the deep ambient crust [62].

We believe we can address this knowledge impasse with a new perspective on crustal microseismicity as substitute for the generic application of fault-centric earthquake slip mechanics to reservoir flow systems in the ambient crust (i.e., away from active faulting). Our observations of microseismicity in the ambient crust (away from active faults) show distinctly different statistical and waveform properties from those attributable to seismic slip action along planar fault surfaces. Statistical and wave spectral evidence from these observations imply that ambient crust seismicity slip deformation occurs within volumetric crustal permeability structures $\kappa(x,y,z) \sim \exp(\alpha\varphi(x,y,z))$ associated with ambient crustal porosity distributions $\varphi(x,y,z)$ [63-67].

While crustal fluid flow has long been putatively associated with cubic-law flow within active or activated quasi-planar structures [42-54], our ambient crustal microseismicity data can be explicitly derived from long-term rock-fluid interactions that generate crustal permeability via the essentially universal spatial correlation empiric of crustal porosity, $S_\varphi(k) \sim 1/k^\beta$, $\beta \sim 1$, recorded in well-log spectra over five decades of wavenumber, 1/km ~ k < 1/cm [68-69].

The power-law scaling spatial correlation nature of crustal porosity, $S_\varphi(k) \sim 1/k$, leads directly to an empirical ambient crust poroperm relation $\kappa(x,y,z) \sim \exp(\alpha\varphi(x,y,z))$ that is lognormally distributed for normally distributed porosity at observed values of scaling parameter α [67,70]. Accordingly, the magnitude distribution of ambient crust microseismicity is more properly regarded as lognormal rather than power-law/fractal [71]. In addition, ambient crust microseismicity is observed to be spatially correlated according to a power-law-scaling two-point spatial correlation function [72-80]. We find the two-point correlation function $\Gamma(r) \sim 1/r^{1/2}$ is characteristic of both crustal permeability and of ambient crustal microseismicity [62]. Finally, ambient crust induced

seismicity waveforms recorded at 2.5km depth in basement rock are dominated by frequencies a decade greater than expected from standard G-R power-law scaling [81]. The observed waveform spectra can be modelled in terms of seismic dislocation slip on spatially complex structures such as permeability $\kappa(x,y,z) \sim \exp(\alpha\varphi(x,y,z))$; as such, the observed and modelled waveform spectra resemble hydrofracture event and acoustic emission spectra rather than standard G-R scaling fault-zone spectra emitted by slip along a smooth planar surface.

Through our observed ambient crust microseismic statistical and waveform properties, we can make testable predictions about the relation of microseismicity to the physical state of crustal volumes. We can logically infer that seismicity stimulated by fluids injected in ambient crust is limited to slip on pre-existing crustal permeability structures of limited physical extent, which thus poses little or no run-away slip seismic hazard [e.g., 30,40]. From a more wide-ranging viewpoint, we can project that natural fluid percolation along long-range poro-connectivity structures persistently emits high-frequency seismic energy at frequencies that are largely outside the standard surface seismic sensor recording range. We thus note that high-frequency seismic energy emission due to fluid flowing in long-range permeability structures can account for the demonstrated ability of multi-channel seismic sensor array data processing to detect and map crustal flow connectivity structures at depth in shale reservoir formations; these perspectives on ambient crustal microseismicity have direct implications for improved extraction of crustal heat [60]. Finally, we can project that the means of creating EGS stimulation fluid pathways lies in incrementing the value of α in the poroperm relation $\kappa(x,y,z) \sim \exp(\alpha\varphi(x,y,z))$. Increasing the value of α is a natural physical process in crustal rock which, in contrast to generating fault-like fluid flow conduits, does little work against the confining stresses [82].

In the ensuing discussion of deep ambient crustal microseismicity observations recorded by sensors at 2.5km depth, we first observe and model instances of spatial correlation and lognormal magnitude distributions for microseismicity in deep basement crust and convective geothermal flow systems. These observed ambient crust microseismicity statistics are identical to the statistics of ambient crustal permeability $\kappa(x,y,z) \sim \exp(\alpha\varphi(x,y,z))$, and prove to be present in the active tectonic province of southern California. We then turn from event statistics to the dynamics of observed waveform spectra to model the slip mechanics within ambient crust permeability structures, finding that slow rupture velocities in localised spatially complex permeability sites $\kappa(x,y,z)$ generate model spectra compatible with deep induced events as well as laboratory-scale acoustic emissions. Our observation and modelling methods result in a coherent perspective on the perceived hazard of induced seismicity, EGS wellbore stimulation, and crustal reservoir flow structure imaging via multi-channel surface seismic array data. .

2. PERMEABILITY CONTROL OF MICROSEISMICITY SIZE AND SPATIAL DISTRIBUTIONS IN AMBIENT CRUST

The material properties of crustal rock include pervasive spatially correlated porosity and permeability structures at all scale lengths whose influence on ambient crust microseismicity has not been adequately recognised and incorporated into microseismicity methodology. Despite the many crustal seismic events associated with quasi-uniform slip on quasi-planar crustal faults over several decades of scale length, it remains an uncomfortable fact that there is little systematic understanding of how crustal faults interact, either during seismic slip or during aseismic periods between slip. Equally there is little observational control of the role of crustal fluids in fault-zone slip activity. As result of lack of systematic diagnostic evidence, what is known about crustal fault interactions and their relation to fluids is largely expressed in the default statistical realm of spatially uncorrelated random fault properties. E.g., the depth, length, height, width displacement, slip rate, dip, strike parameters of faults embedded in a quasi-elastic continuum are generally fixed by sets of uncorrelated random numbers [55-56, 58-59]. In like manner, crustal fluids are treated as a passive random mechanical partner in distributing stress within the faulted medium [e.g., 54]. Standard models of far-field stress on crustal fault systems are computed by taking statistical means over spatially uncorrelated fault properties that are not subject to large scale spatially unpredictable fluctuations [e.g., 48-49].

Amidst the plethora of uncorrelated randomness, the single organising principle affecting crustal faults is the Gutenberg-Richter (G-R) fractal relation between fault size L and fault number N, $N(L) \sim N_0 (L_0/L)^d$. The physical constraint imposed by the G-R fractal is, however, weak. The G-R fractal distribution of slip event sizes is compatible with an essentially arbitrary range of physical interactions involving crustal faults, fluids, and stresses. Attempts to define a range of G-R fractal scaling exponents have not generated convincing results [83].

By contrast to fault-zone seismicity observation, the st1 Deep Heat induced seismicity data set from fluid injection at 6km depth in stable crystalline basement rock recorded by vector sensors at 2.5 km depth provides a wealth of detail for microseismic mechanics in the stable ambient crust [30]. Under stimulation by controlled fluid injection, the microseismicity data show that crustal seismicity in the deep stable crust is both spatially correlated and lognormally distributed [61-62]. To these two primary observations we add the third observation, that these microseismic event spatial correlation and event size distribution properties accord closely with the spatial correlation and magnitude distribution properties of crustal permeability.

Figs 1-3 illustrate how the standard Gutenberg-Richter (G-R) fractal distribution of microseismicity events only loosely ties to the wellbore, well-core, and well-production poroperm empirics that define crustal rock-fluid interactions. In Fig 1, we see the traditional application of the G-R fractal relation to microseismicity recorded at convective geothermal fields in Indonesia: the logarithm of event numbers $N(m)$ plotted on the vertical axis against the event magnitudes m on the horizontal axis. The microseismicity event magnitudes and numbers are plotted in two formats. Red squares show the cumulative number of events with magnitudes greater than the magnitude shown on the horizontal axis; blue crosses give the actual event count observed for each magnitude interval along the horizontal axis.

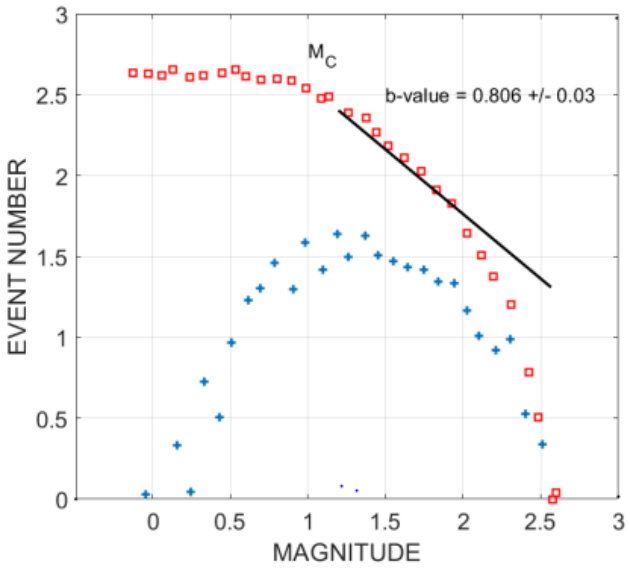

Fig 1 – The numerical distribution of microseismicity event magnitudes recorded in an Indonesian geothermal field [39]. Blue crosses give the observed number $\log_{10}(N)$ of events for half-magnitude intervals; red squares give the cumulative numbers $\log_{10}(N)$ of events above a given magnitude value. The straight-line fit to the cumulative event numbers at magnitudes above m ~ 1 gives the b-value associated with the Gutenberg-Richter relation $N(m) \sim 10^{-bm}$, for magnitudes m. M_C denotes the magnitude above which it is assumed that all microseismic events that occur in the survey volume are in fact detected by the survey network. In the past, the decline in number of recorded events has been attributed to purely observational deficiency. In fact, the decline in recorded events can be quantitatively matched to a natural decline in event numbers due to microseismic slips event occurring on pre-existing permeability structures that have a natural decline in permeability value. The same decline in permeability is observed in well-productivity distributions [e.g., 64].

Figs 2-3 show how both the Fig 1 accepted event count at higher magnitudes and the interpreted ''missing'' event counts at lower magnitudes are naturally accounted for in terms of observed crustal properties. Well-log, well-core and well-productivity data show that typical crustal volumes host a population of permeability structures $\kappa(x,y,z) \sim \exp(\alpha\varphi(x,y,z))$ derived from a population $\varphi(x,y,z)$ of normally-distributed spatially-corrected porosities and fixed by the value of poro-connectivity parameter α. In Fig 2 the histogram operation $H(\kappa) \equiv H(\exp(\alpha\{\varphi\}))$ gives the statistical population distributions of crustal permeability as a function of the degree of spatial poro-connectivity α. The blue curves fit through Fig 2 numerical distributions are formal lognormal distributions given by specific means μ and variances σ^2. The fits numerically demonstrate that each computed permeability population $\kappa(x,y,z) \sim \exp(\alpha\varphi(x,y,z))$ is effectively lognormally distributed with the degree of lognormality or skewness as defined by parameter α.

Fig 2 numeric modelling is based on a large population of suitably scaled random numbers representing a normally distributed population of crustal porosities $\{\varphi\}$ of minimum value 0.1 and mean value $\underline{\varphi} \sim 0.2$. Without regard to spatial organisation of the porosity, we display the associated permeability frequency distributions given by histograms of permeability function $H(\kappa) \equiv H(\exp(\alpha\{\varphi\}))$ for poro-connectivity parameter α values [5 15 20 30]. The left-hand plots show the four permeability distributions on linear axes; the right-hand plots use logarithmic axes. Blue dots denote the $H(\exp(\alpha\{\varphi\}))$ distributions; red traces denote lognormal probability distribution function fits to the $H(\exp(\alpha\{\varphi\}))$ distributions. The lognormal distribution fit mode values (most frequent values) are respectively [0.38 0.17 0.1 0.04], with median values (50% above, 50% below) respectively [0.41 0.20 0.14 0.06].

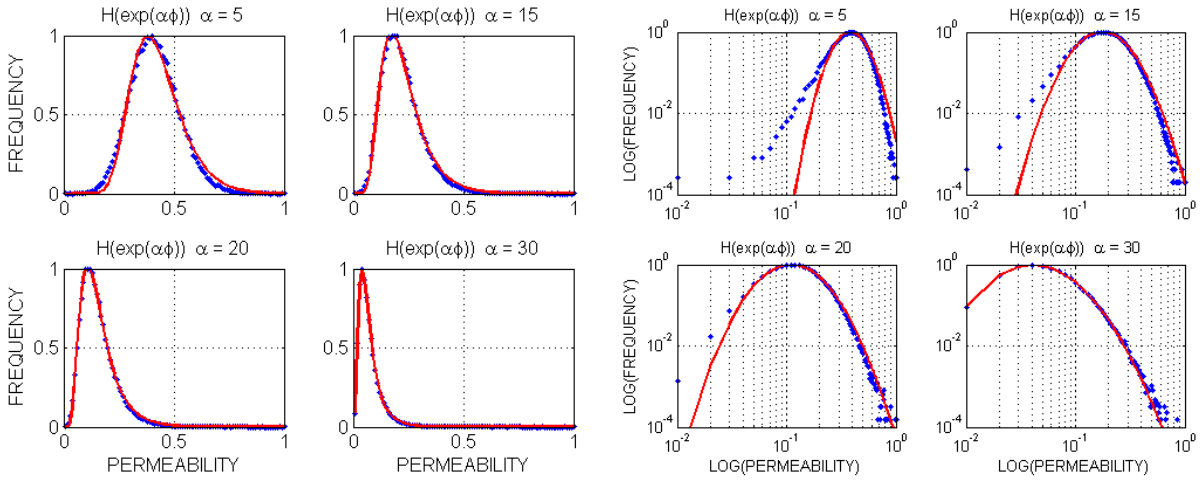

Fig 2 – Numerical simulation of crustal permeability distributions arising from the poroperm relation $\kappa(x,y,z) \sim \exp(\alpha\varphi(x,y,z))$. (Left) Linear and (right) loglog plots of permeability frequency versus permeability given by histograms $H(\exp(\alpha\varphi))$ for four values of poro-connectivity parameter α = [5 15 20 30].

For small α ~ 5 in the upper-left Fig 2 plots, H(κ) is normally distributed as mathematically required by the expansion, {κ} ~ exp(α{φ}) ~ 1 + α{φ}. For values α ~ 15 and higher the Fig 2 numerical permeability distributions are lognormally skewed. For the ambient crust, well-core data from reservoir and basement rock establish the empirical condition α$\underline{\varphi}$ ~ 3-5, where $\underline{\varphi}$ is the mean formation porosity [67]. Applied to the Fig 2 numerical computation, the α$\underline{\varphi}$ ~ 3-5 empirical condition corresponds to α with values 15 and above. The frequency distribution of well-productivities for all types of crustal fluids is observed worldwide to be lognormal, conforming to the α$\underline{\varphi}$ ~ 3-5 empirical condition on crustal permeabilities.

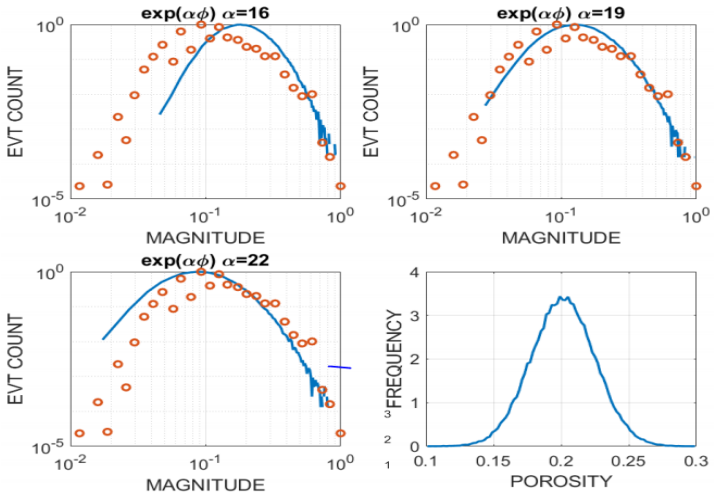

Fig 3 – Fitting the H(exp(αφ)) distribution to Fig 1 distribution of Indonesian geothermal field microseismicity. The porosity φ distribution of mean porosity $\underline{\varphi}$ = 0.2 is in the lower right plot; remaining plots match H(exp(αφ)) distributions to observed magnitude distribution for poro-connectivity values α = 16, 19, 22. The best fit is for α = 19; this value meets the empirical condition α$\underline{\varphi}$ ~ 3-5 observed worldwide for crustal permeability [67].

The results of Fig 2 invite us to apply the mathematical form H(exp(α{φ})) to frequency distributions of ambient crust microseismic magnitudes. Fig 3 applies the H(exp(α{φ})) numerical model to the Fig 1 magnitude distribution of microseismicity recorded in Indonesia. The best fit value of poro-connectivity parameter is α ~ 19, for which α$\underline{\varphi}$ ~ 3.8 meets the empirical α$\underline{\varphi}$ ~ 3-5 criterion observed for poroperm properties in the ambient crust. A further H(exp(α{φ})) model-fitting data example is given in Fig 10 (left).

A higher order statistic than population distribution is the internal spatial correlation of microseismic events given by the two-point correlation function. If event locations are spatially uncorrelated then the two-point correlation function is flat as in the function of event separation r, Γ(r) ~ $1/r^0$ ~ const. If event locations are correlated, then any particular event will have either more or fewer events at a given distance than expected from uncorrelated randomness. It is of great interest to find if such spatial correlations exist, and if they exist, to find if they systematically scale by power-law dependence on spatial offset r. As crustal permeability spatial distributions arise from the essentially universal systematic spatial correlation empiric of crustal porosity, $S_\varphi(k) \sim 1/k^\beta$, β ~ 1, over scales lengths from cm to km [68-69], Figs 1-3 imply that we should not be surprised to find a power-law spatial correlation between microseismic event-pair offsets r.

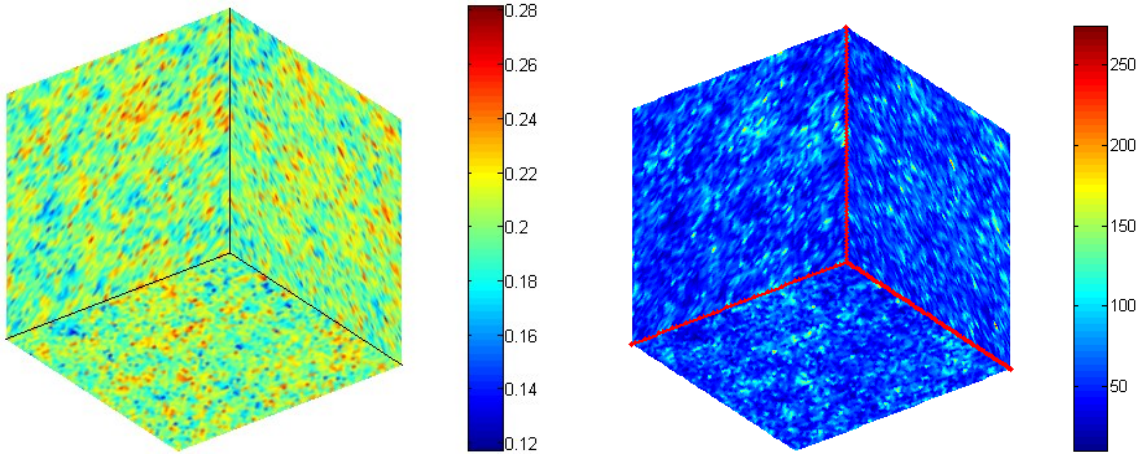

Fig 4 – (Left) Numerical realisation of spatially-correlated porosity distribution φ(x,y,z); the spatial correlation is such that logging a wellbore through the porosity field will record spatial fluctuations φ(z) such that the Fourier spectral power scales inversely with spatial frequency k, $S_\varphi(k) \sim 1/k^\beta$, β ~ 1. (Right) The associated permeability field κ(x,y,z) ~ exp(αφ(x,y,z)) for α = 20 (arbitrary units).

Figs 4-11 provide computational evidence for a systematic spatial correlation function, Γ(r) ~ $1/r^{1/2}$, for both crustal permeability sites and for microseismicity events. Where uncorrelated random distributions of sites/events imply that a neighbour site/event is equally likely at any given offset r, we will see that probability of finding a crustal permeability or seismic slip event site at distance r from a given site/event systematically declines with the square-root of the site/event offset distance r. As with Figs 1-3, the key feature here

is that in the ambient crust, permeability and seismic slip event locations have the same spatial correlation property. This statistical congruence implies an underlying physical connection between crustal permeability and crustal seismic slip events.

Fig 4 numerically illustrates the spatial distribution properties of porosity and permeability in a crustal volume. The porosity spatial distribution $0.12 < \varphi(x,y,z) < 0.28$ at left is such that a linear wellbore through the numerical volume returns a sequence of values with spectral power that scales inversely with spatial frequency over 8 or 9 octaves, $S_\varphi(k) \sim 1/k^\beta$, $\beta \sim 1$. We recall that in contrast a numerical volume of uncorrelated porosity values has a flat power spectrum, $S_\varphi(k) \sim 1/k^\beta$, $\beta \sim 0$. The associated permeability spatial distribution $\kappa(x,y,z) \sim \exp(\alpha\varphi(x,y,z))$, $\alpha = 20$, shown at right in arbitrary units has a number of localised high value regions that are both porous – i.e., have low cohesive strength -- and permeable – i.e., readily subject to pressurisation by injected fluid.

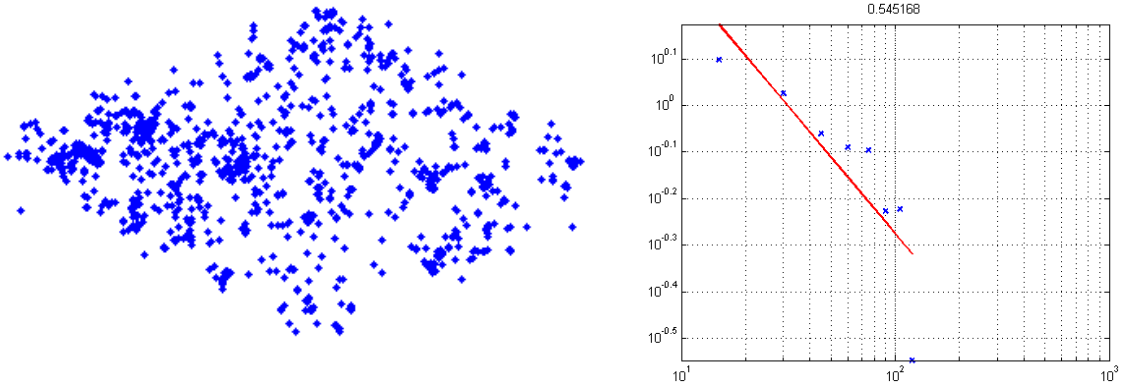

Fig 5 – (Left) Spatial distribution of high-porosity/high-permeability sites for a slice through the Fig 4 numerical permeability field. The high permeabilities make it logical that these sites are subject to entry by injected high pressure fluids; the high porosities make it logical that these sites are locally weak; together these conditions make it logical that local stress heterogeneities cause Coulomb failure at these sites. (Right) Two-point spatial correlation function of left-hand sites of high seismic slip potential; the observed slope on the loglog plot corresponds to the function $\Gamma(r) \sim 1/r^{1/2}$ over a decade range of site-offset.

If we inject the Fig 4 permeability volume with high pressure fluid, a number of localised sites in the volume will have greater amounts of mobile pressurised fluid than others. Such localised high flow locales are plotted in Fig 5 (left). Elevated fluid pressures at the sites of low cohesive strength located in this plot meet the criterion for Coulomb slip failure and hence are logical sites for seismic activity in the pressurised crustal volume. A loglog plot of the two-point correlation distribution for this high porosity/permeability population is given in the Fig 5 (right). The correlation function is approximately $\Gamma(r) \sim 1/r^{1/2}$ over a decade of site offsets r. A Matlab version of the two-point-correlation algorithm is appended.

Fig 6 illustrates the event distribution of microseismicity recorded in an Indonesian geothermal field [62], with Fig 7 showing the event-event spatial correlations of the observed microseismicity to scale inversely with the square root of the event-event offset r.

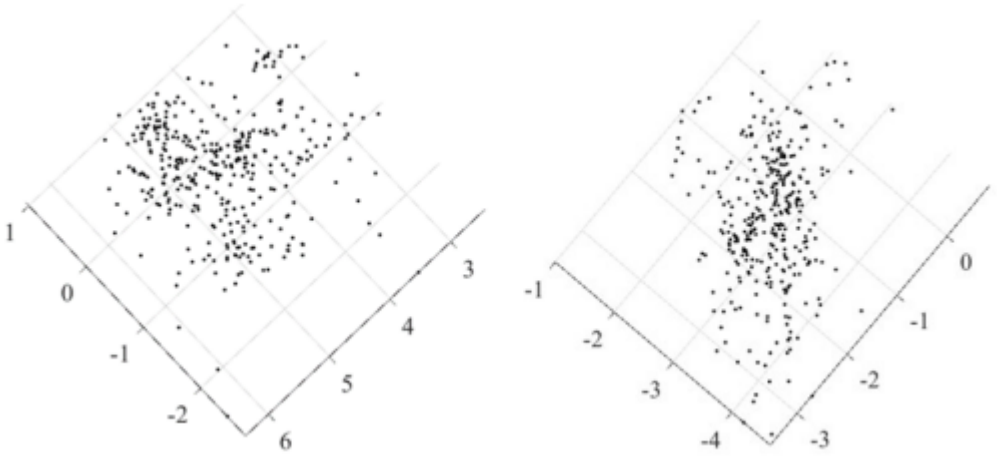

Fig 6 – Spatial distribution of microseismicity in two Indonesian geothermal fields [62]. The two-point correlation function applies to these event locations is given in Fig 7.

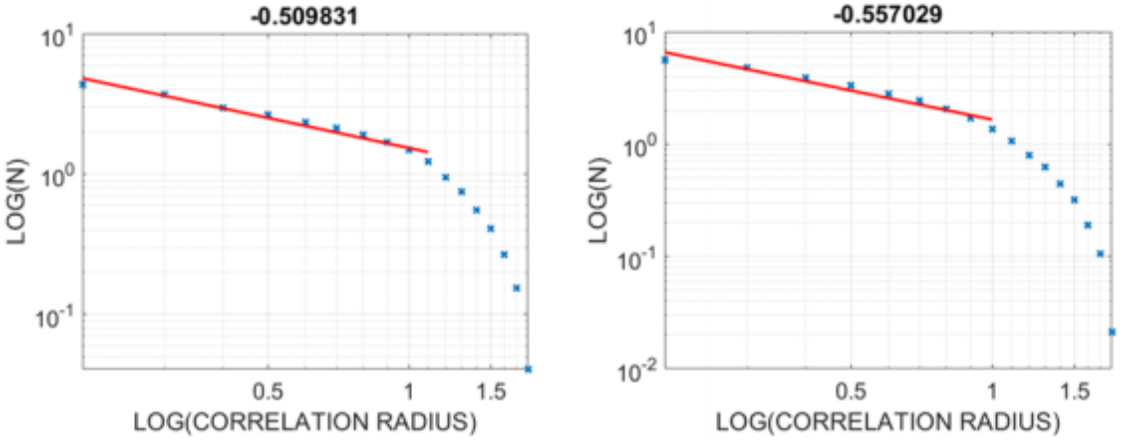

Fig 7 – Loglog plots of two-point correlation function for spatial distribution of microseismicity events recorded in two Indonesian geothermal fields (see Fig 6). The straight-line portion of the computed correlation function is consistent the power-law distribution $\Gamma(r) \sim 1/r^{1/2}$ illustrated in Fig 4-5 for spatial correlations of high-porosity/high-permeability spatial site locations generated by the empirical crustal poroperm distribution $\kappa(x,y,z) \sim \exp(\alpha\varphi(x,y,z))$ for values $\alpha \sim 20$.

Figs 8-11 extend the Figs 1-7 statistical property analysis to the southern California tectonic province. Fig 8 shows the largely fault-controlled distribution of year 2010 southern California microseismicity registered in Index of /ftp/catalogues/SCSN [*service.scedc.caltech.edu* › ftp › catalogs › SCSN].
Fault-controlled linear trends are evident in most seismicity clusters, but the cluster in red expanded in Fig 9 shows a sequence of more rounded seismicity distributions. The events of the more rounded event cluster are likely to be less controlled by a central fault and more likely to be controlled by local ambient crust poroperm distributions.

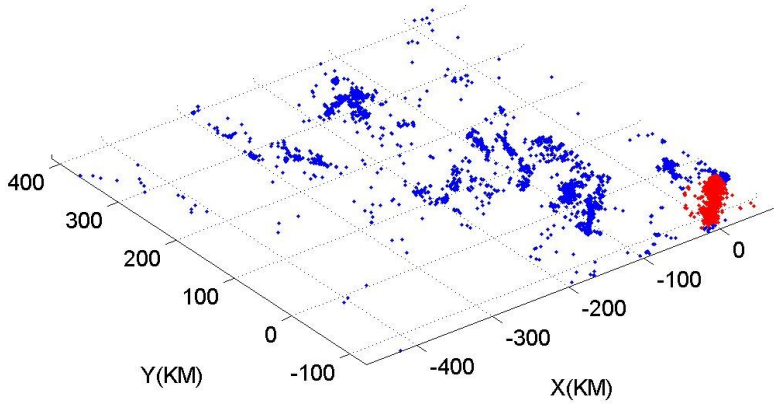

Fig 8 – Spatial distribution of crustal microseismicity in southern California for year 2010 [Index of /ftp/catalogues/SCSN].

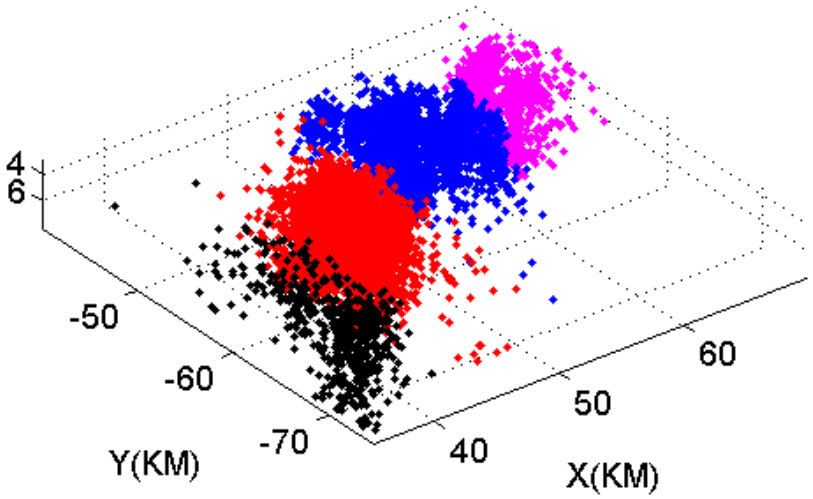

Fig 9 – Expanded view of spatial distribution of the portion of southern California year 2010 microseismicity given in red in Fig 8. The rounded spatial distributions are centred along an active fault trend, but the laterally extensive off-fault event populations are logically controlled by ambient crustal fluid-rock interaction permeabilities. Fig 10 results bear out this expectation.

The southern California microseismicity clusters are an order of magnitude larger in areal extent than the st1 Deep Heat basement site and the Fig 6 Indonesia geothermal site clusters, and result from slow ongoing tectonic crustal deformation rather than rapid fluid injection or convective fluid circulation. Nonetheless, the Fig 10 statistical properties of the Fig 9 event population show that these tectonically induced seismicity clusters have the same statistical distribution and spatial correlation properties as the smaller-scale fluid-activity clusters and Figs 4-5 synthetics.

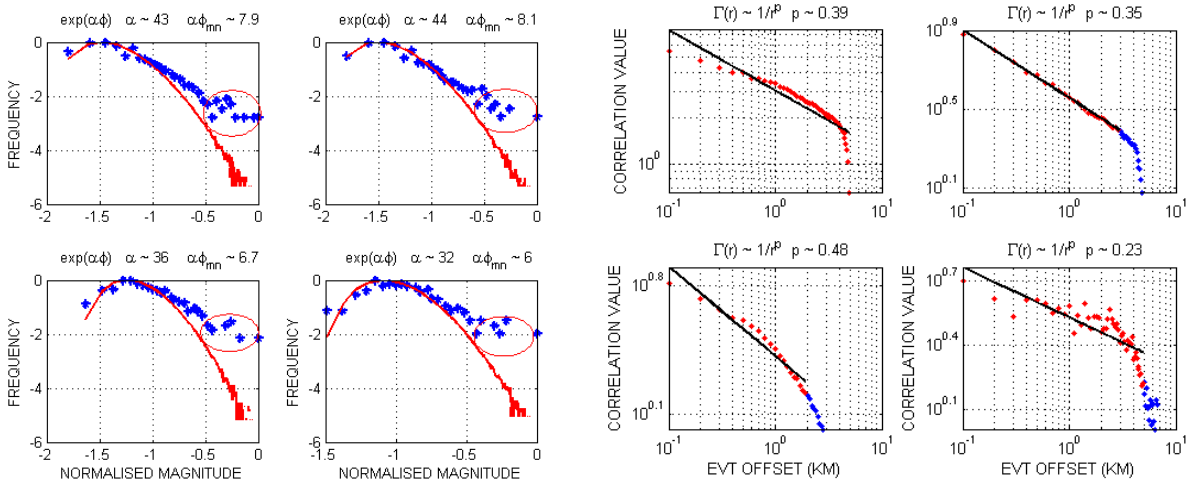

Fig 10 – (Left) Lognormal frequency distributions of four spatial clusters of southern California microseismicity in Fig 9. Blue dots are normalised microseismicity event counts; red curves are best-fit histogram distributions for crustal permeability exp(αφ(x,y,z)). Events marked by ellipses are population increases due to the embedded tectonic fault running through each cluster group. (Right) Loglog plots of spatial correlation distribution of events in each of Fig 9 clusters. The straight-line fits approximate the correlation function Γ(r) ~ 1/r$^{1/2}$.

The exception to the general conclusion about Fig 10 statistical distributions for southern California tectonic seismicity in Fig 9 is indicated by red ellipses at higher magnitudes in the left-hand plots. At higher event magnitudes, the internal fault system running through the microseismicity clusters produces an excess of seismic activity over that given by crustal permeability distribution fits. Excesses of higher magnitude events over the number expected for crustal permeability are more pronounced for the Fig 8 microseismicity clusters more noticeably aligned along tectonic faults.

In Fig 10, the flatter the straight-line fit to higher magnitude frequency distributions (e.g., Fig 1), the lower the G-R power-law b-value exponent $N(m) \sim 10^{-bm}$. From the evidence of Fig 10 (left) event counts marked by ellipses, we see that G-R relation b-value is physically rooted in the distribution of crustal permeability structures controlled by the poro-connectivity parameter α. Referring to the right-hand loglog plots of Fig 2, b-values decrease as α increases. As α increases, permeability structures become more spatially correlated until, as in Fig 10, the increased spatial correlation becomes associated with seismic activity on tectonic faults within the clusters. Per our discussion of higher magnitude events, it bears repeating that the long-ignored frequency distribution of low magnitude events properly physically accounted for by the ambient crust permeability structures κ(x,y,z) ~ exp(αφ(x,y,z)) with values of the empirical parameter α ~ 20 in the appropriate range.

As a final instance of microseismicity statistical distributions, Fig 11 shows that the spatial distribution of st1 Deep Heat events stimulated by fluid injected at 6km depth in Finnish basement is correlated over a 50-to-400 meter range according to Γ(r) ~ 1/r$^{1/2}$ in accord with Fig 5 synthetic permeability distributions, Fig 7 distributions of geothermal field microseismicity, and Fig 10 distributions of southern California seismicity.

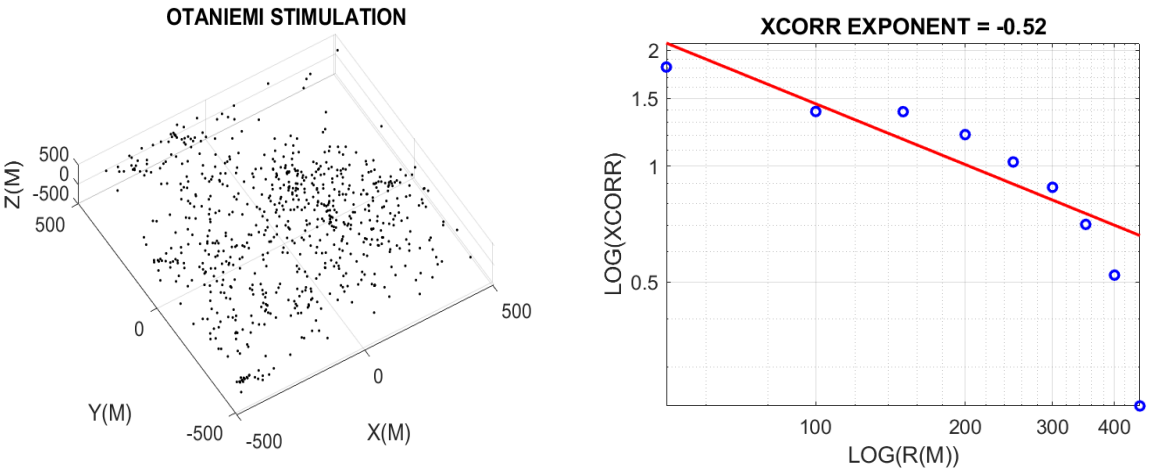

Fig 11—(Left) Spatial distribution of microseismic events stimulated by fluid injected at 6km depth in Finnish basement rock. (Right) Two-point spatial correlation distribution approximates the function Γ(r) ~ 1/r$^{1/2}$ over spatial offset range 50-400 meters.

With Figs 1-11 we establish a correspondence between (i) wellbore, well-core, and well-productivity properties for crustal porosity and permeability, (ii) numerical simulations of porosity and permeability distributions, and (iii) spatial distributions of microseismicity at Hm scales in deep crystalline basement rock, km scales in convective geothermal systems, and 10km scales in the southern California tectonic province. The correspondence between crustal permeability and crustal microseismicity over 2 decades of scale length and a range of geological settings makes plausible that much ambient crustal seismicity is associated with crustal permeability structures rather than slip on planar faults.

Beyond the statistical evidence of three field data sets, only the st1 Deep Heat crystalline basement seismicity was observed at sufficient proximity to record accurate details of the induced seismic radiation field. The basement event seismic emissions do not conform to what might be expected if the seismic slip occurred on planar fault structures. We next look at how crustal permeability relates to high frequency waveforms emitted by seismicity induced at 6km depth and recorded at 2.5km depth, and by hydrofracture events generated and recorded at 2.5km depth.

3. CRUSTAL PERMEABILITY STRUCTURE DEFORMATION AS SOURCE OF INDUCED SEISMICITY HIGH FREQUENCY WAVEFORMS

A very considerable gap exists between the spectral distribution of waveform frequency amplitudes observed for the deep basement stimulation microseismicity and seismic emissions of a standard fault slip. In Fig 12, black traces show the waveform spectra across the observed magnitude range $-1 < m < 2$ and red traces show notional spectral distributions such as $u(f) \sim u_0 /(1 + (f/f_0)^2)$ expected for fault slip seismic waveforms. The observed seismic waveform peak frequency $f_0 \sim 500$Hz is up to a decade higher than expected for fault slip processes at these magnitudes, and there is no evidence in the observed spectra for the standard frequency scaling with fault dimension $f_0 \sim 1/L$ found in fault slip seismicity.

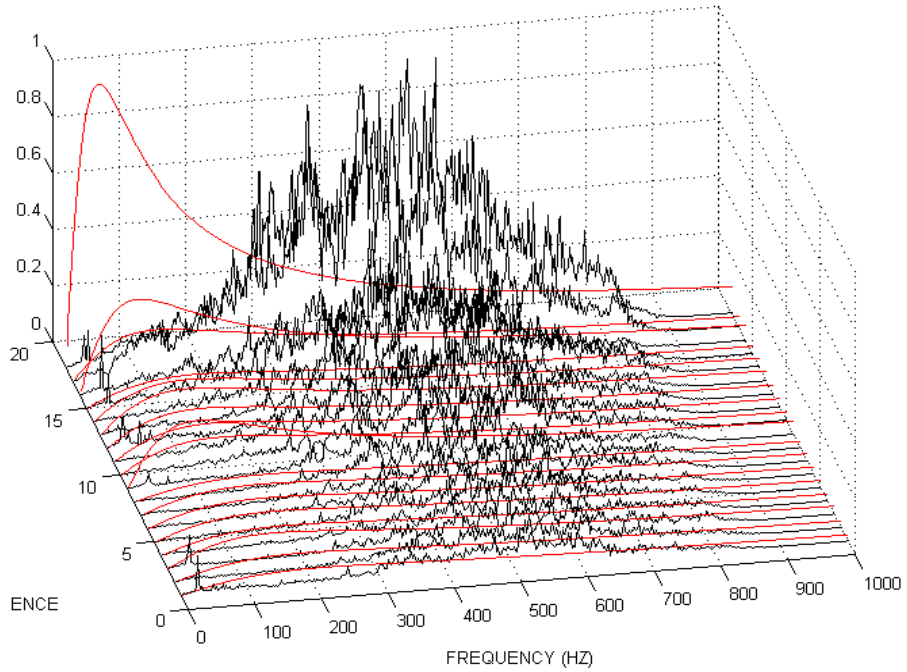

Fig 12 – (Black) Sequence of waveform amplitude spectra for microseismicity in magnitude range $-1 < m < 2$ induced by fluid injection at 6km depth in crystalline basement and recorded at 2.5km depth by a seismic sensor array. (Red) Notional spectral distributions for fault-slip event source motion for observed magnitude range; observed peak energy does not occur at characteristic frequencies f_0 that scale with event magnitude.

In addressing the Fig 12 seismic spectra discrepancy, we follow the pioneer account given in three papers by Norman Haskell of elastodynamic radiation generated by fault-zone displacement slip events [13-15]. Haskell's initial paper noted that model seismic radiation due to a smoothly propagating slip front of velocity approaching the shear-wave velocity, $V_{slip} \sim V_S$, over faults of length L gave radiation spectra for low frequencies associated with slip duration $T \sim L/ V_{slip}$ but did not produce abundant high frequency radiated energy according with observation. In consequence of model high frequency deficiency, Haskell's second paper introduced fault roughness allowing for episodes of high frequency seismic emission during a dislocation slip proceeding at a mean velocity $V_{slip} < V_S$. A generic parameter form of fault zone roughness showed that high frequency energy could be included in the radiation spectra while matching the spectra at low frequencies. With an increasing number of seismic waveforms recorded by seismic stations near rupturing faults, a third Haskell paper responded with numerical models for waveforms per se rather than being limited to modelling waveform spectra. Using Haskell's waveform modelling procedure, Kanamori [16] and Trifunac [17] used trial-and-error fault-zone slip event functions to match seismic waveforms recorded for regional earthquakes. Subsequently it became routine to use Haskell's methods to match suites of fault-zone earthquake waveforms to find explicit fault-zone rupture processes [18-22].

We replicate the Haskell modelling path by exploring generic seismic radiation waveform spectra in terms of emissions from spatially complex dislocation slip processes. While Haskell made do with hypothetical fault zone complexities, we have the crustal physical complexity given by the permeability distributions $\kappa(x,y,z) \sim \exp(\alpha\varphi(x,y,z))$ discussed in §2.1. As such sources generate waveforms too complex to match observed waveforms, we use Haskell mechanics to compute spectral distributions of displacement velocity

waveforms emitted by 2-dimensional deformation fronts progressing through generic 3-dimensional permeability structures κ(x,y,z). Fig 13 illustrates our spectral distribution modelling results.

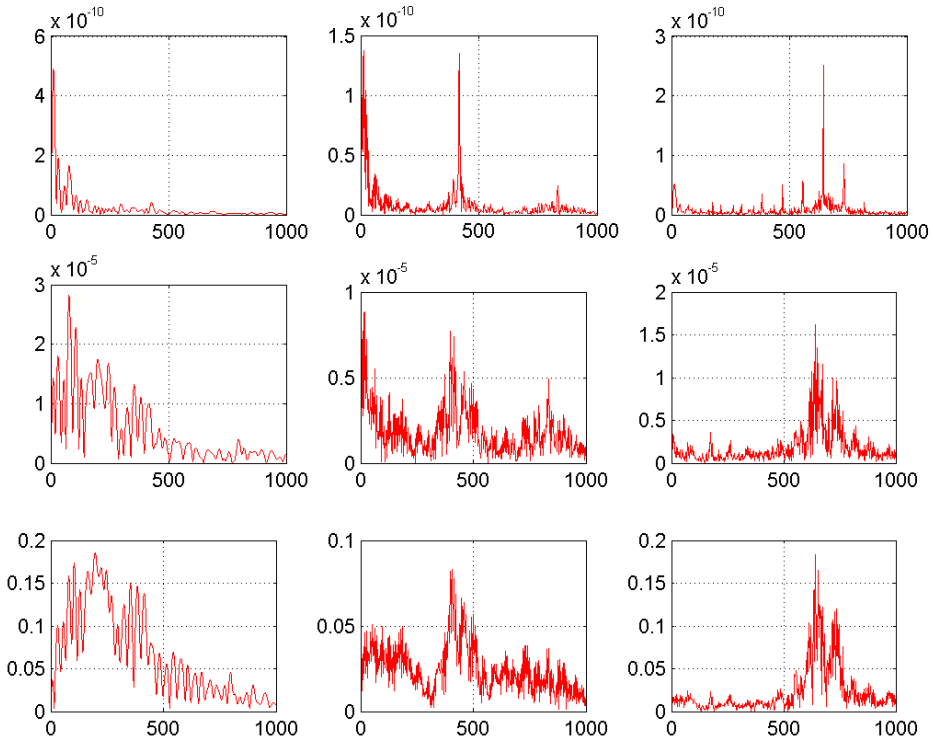

Fig 13 – A 3 x 3 array of model spectral amplitude distributions for waveforms emitted by a slip dislocation front traversing a crustal permeability volume κ(x,y,z) ~ exp(αφ(x,y,z)). The array models are defined by a range of mean slip velocities $V_S > V_{slip} > V_S/10$ (left to right) and a range of poro-connectivity parameters 5 < α < 30 (top to bottom). The upper-left-most model most nearly resembles a fault surface with low-correlation complexity allowing rapid slip advance. The lower-right-most model resembles a poorly defined fault-surface with a large degree of internal spatial correlation allowing only low velocity mean slip velocity.

Following Haskell, the seismic slip deformation front can in principle traverse a crustal volume κ(x,y,z) for a range of mean slip velocities V_{slip}. The mean slip velocity determines how radiation from individual patches of the permeability structure κ(x,y,z) combine to create a net seismic radiation waveform. The spatial organisation within the permeability structure will also affect how radiation from individual source patches combine to generate the observed waveform. Our spectral modelling allows for a range of effective rupture front velocities $V_S/10 < V_{slip} < V_S$ moving along an arbitrary plane through crustal permeability source volumes of characteristic dimension L. In parallel to a range of slip event velocities, the model permeability structures are defined over a range spatial-connectivity parameter values 5 < α < 30 applied to normal porosity distributions with mean $\underline{\varphi} \sim 0.2$ (e.g., Fig 4). The low value α ~ 5 is well below the empirical crustal permeability condition $\alpha\underline{\varphi} \sim 3\text{-}5$; the highest value α slightly exceeds the empirical condition.

We see in Fig 13 that the range of effective slip velocities ($V_S/10 < V_{slip} < V_S$) and permeability poro-connectivity parameters (5 < α < 30) produces distinct radiation waveform spectral distributions in line with Haskell's analysis of moderating fault zone slip velocities and roughness. At the upper left, high effective slip velocities $V_{slip} \sim V_S$ traverse permeability structures with low degrees of spatial correlation for parameter α ~ 5 to produce waveforms in which radiation is coherent at low frequencies and destructively incoherent at high frequencies. This model compares generically with the red traces in Fig 12.

By contrast, at Fig 13 lower right low effective slip velocities $V_{slip} \sim V_S/10$ traversing permeability structures having high degrees of spatial correlation parameter given by α ~ 25 produces waveforms in which radiation destructively interferes at low frequencies but generates an abundance of incoherent radiated energy at high frequencies. Such models compare generically with the observed black spectral traces of Fig 12.

For Fig 13 modelling specifics, the plotted elastodynamic radiation waveform spectral distributions are computed for a transverse particle displacement field $u(r,t+r/V_S)$ recorded at retarded time $t+r/V_S$ for a sensor at far-field distance r >> L from a crustal source permeability distribution κ(x,y,z) of dimension L. The radiation displacement field $u(r,t+r/V_S)$ sums over a source point dislocation velocity field $\underline{\mathring{D}}(x,y,z,t)$,

$$u(r,t+r/V_S) \sim A/4\pi V_S \iiint dV\ \Gamma/r\ \underline{\mathring{D}}(x,y,z,t), \qquad (1)$$

where A is a slip surface of dimension L along which seismic slip occurs through the permeability volume, V_S is the crustal shear wave velocity, Γ is the appropriate sensor-source geometric radiation factor for slip along surface A as recorded by sensor location at distance r, and the volume integration sums over all elements of the source slip velocity distribution on surface A. Slip on A occurs over source action time interval 0 < t < T, where slip duration $T \sim L/V_{slip}$ occurs over length L along surface A at mean slip velocity V_{slip}. For simplicity, we consider a source volume of characteristic dimension L and set Γ = 1, $A = L^2$, and associate the slip velocity

distribution within the crustal permeability volume as occurring on a slip front of mean amplitude $\underline{\mathring{D}}_0$ progressing linearly with time through the permeability zone of dimension L. The slip source function is thus $\underline{\mathring{D}}(x,y,z,t) \sim \underline{\mathring{D}}_0\ W(x,y,z)\ t/T$, where $W(x,y,z) \sim \exp(\alpha\varphi(x,y,z))/\max(\exp(\alpha\varphi(x,y,z)))$ is the normalised weight distribution that captures the spatial complexity of crustal permeability spatial fluctuations in the volume L^3, and $\underline{\mathring{D}}_0$ expresses the velocity of the deformation front given as the characteristic mean speed.

In Fig 13 we have in generic terms the result we are seeking: a physical characterisation of the rupture fronts that generate the microseismicity waveform spectra observed in Fig 12 black traces that is expressed in physical terms consistent with the congruent ambient crust poroperm and microseismicity statistical properties presented by Figs 1-11. The desired spectral distributions correspond to a slow rupture velocity moving along a surface of strongly correlated roughness. The generic model spectral distributions also duplicate the Fig 12 standard fault-like slip waveform spectral distributions shown in red for the case of rapid slip on a planar surface of uncorrelated roughness.

The Fig 13 model spectra indicate that observed ambient crust microseismic slip occurs, not on ever smaller versions of a fault-slip surface as suggested by the standard G-R fractal, but over the range of lognormally distributed and spatially correlated permeability fabric of ambient crustal rock. In the absence active faults, injected stimulation fluids track pre-existing poro-connectivity percolation pathways to disturb the fluid-rock stress equilibrium and trigger slip at high-porosity/high-permeability sites. Fig 13 modelling indicates that seismic slip at these sites emits higher frequency energy than is expected for fault-slip events. The high frequency waveforms in the range of 500Hz are not typically recorded by surface or near-surface sensors. Lack of surface high-frequency data for subsurface induced seismicity may be due to weakness of the high frequency emissions, or high frequency wave scattering and delay due to near-surface conditions, or failure to record data at the necessary sampling rates.

A comparable set of high frequency seismic stimulation events recorded at 2.5km depth supports the Fig 12-13 ambient basement rock induced microseismicity waveform spectra and their interpretation as slip on crustal high permeability sites. A programme of hydrofracture observation conducted in western Colorado tight gas sands acquired data from a 240m-long 30-fold 3C accelerometer array grouted into a vertical wellbore with array centre at the hydrofracture stimulation depth [84-86]. Multiple hydrofractures were conducted over a period of weeks, with the ensuing microseismicity recorded for periods of hours. The hydrofracture slip occurred along the strike of the regional maximum principal horizontal stress. Fig 14 shows a quartet of observed array waveforms across the sensor array.

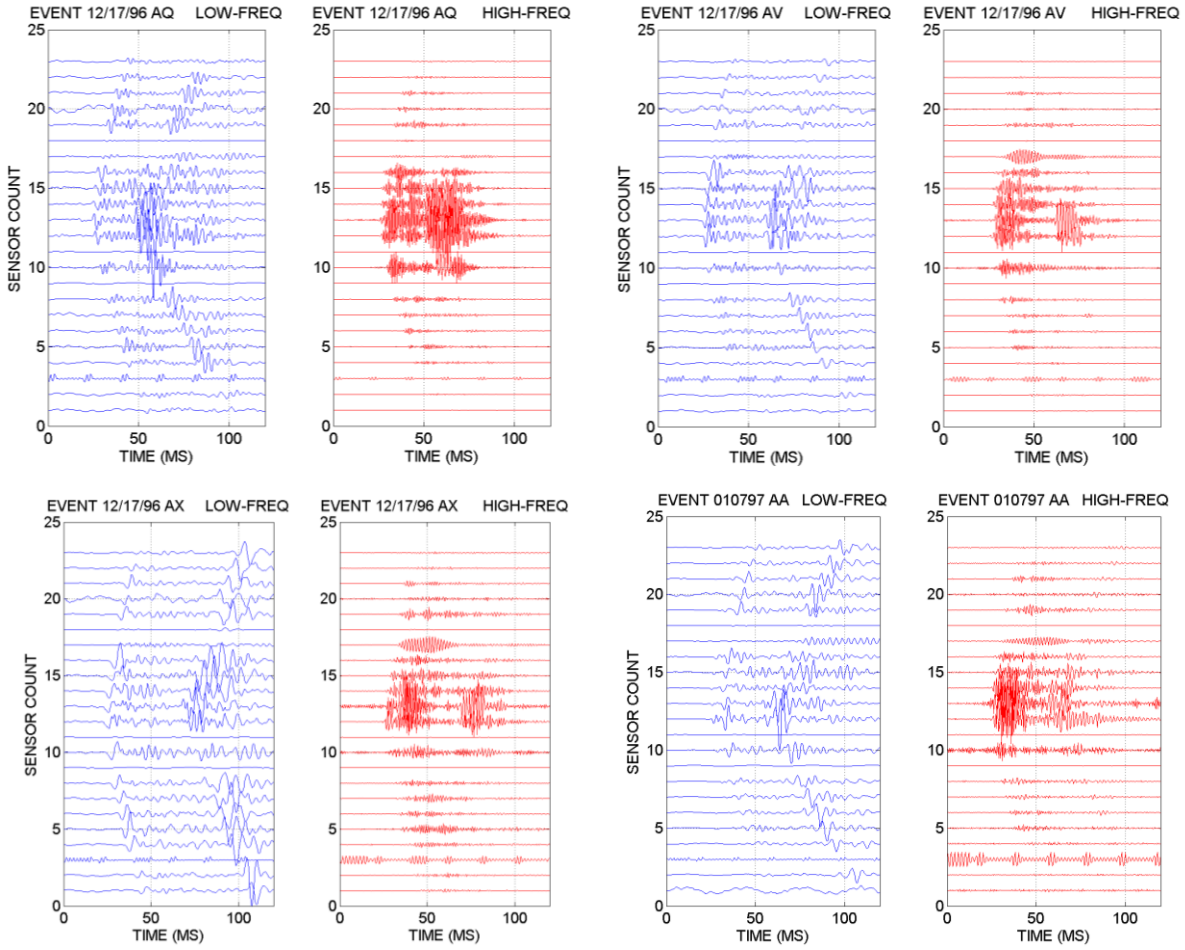

Fig 14 – Seismic waveforms recorded by a vertical array of grouted accelerometers for hydrofracture-induced seismic slip events at 2.5km depth in western Colorado tight gas sands [84]. The vertical array spans 240 meters at ~ 100-meter offset from the hydrofracture event. Blue waveforms are low-pass filtered and red waveforms high-pass filtered at 200Hz. Blue waveforms have discrete P- and S-wave pulses consistent with seismic radiation from dislocation slip induced on a fracture plane; red waveforms indicate radiation from a more complex slip distribution. The fidelity of the P- and S-wave pulses indicates high frequency sensor stability.

Array waveforms for selected events are given in passbands above and below 200Hz. At left in blue, the waveforms below the 200Hz filter cut-off show distinct P and S phases moving across the accelerometer array away from mid-array sensor at the hydrofracture depth. Waveforms above 200Hz cut-off in red at the right show 500-1000Hz wave energy clustered at the level of the hydrofracture event. The waveform filter gives clear evidence for two substantially different slip functions: in blue, the source function has the properties of slip on a smooth fault surface; in red, the slip function generates high frequency P and S waves directed at the mid-sensor level rather than moving across the array. Collectively the waveforms indicate radiation from a hydrofracture fault plane embedded in heterogeneous crustal volume.

Characteristic waveform amplitude spectra for the two slip types are shown in Fig 15. Allowing for lower sensor response at low frequencies, the blue spectral amplitudes are consistent with dislocation slip motion on a planar surface as indicated by the red traces in Fig 12 and the model spectra at the upper left of Fig 13. In contrast, the red spectral amplitudes are consistent with complex slip motion on an irregular surface as given by the black traces of Fig 12 and the model spectra at the lower right of Fig 13.

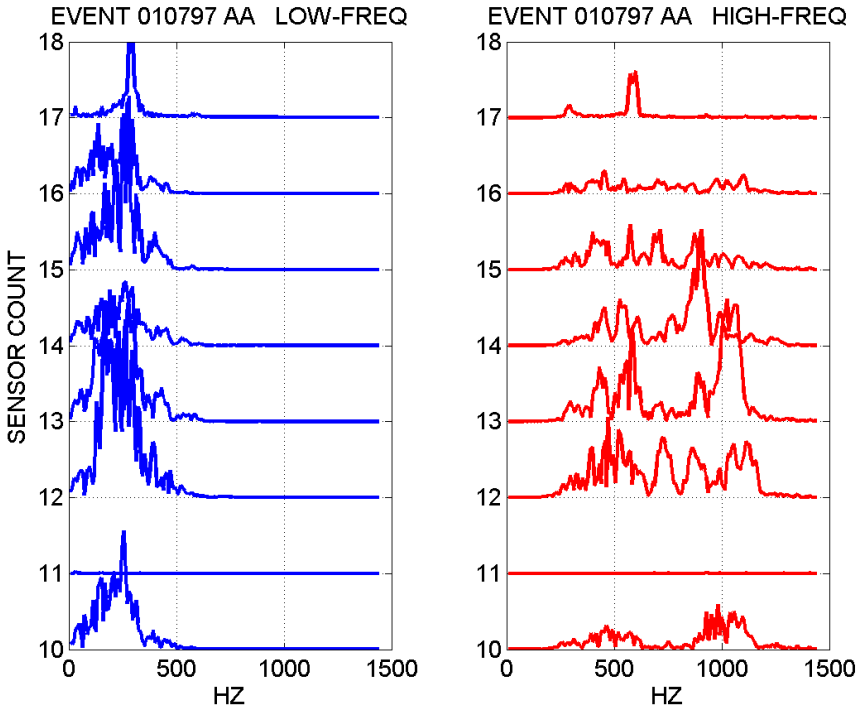

Fig 15 – Amplitude spectra for the central level sensor waveforms shown in Fig 14 lower right. The frequency content below 200 Hz is due to distinct P- and S-wave pulses radiating away from a fault-like slip event induced by injected hydrofracture fluids as modelled at upper left in Fig 13; the low spectral amplitudes at lowest frequencies is due to limited low frequency sensor response. The frequency content above 200 Hz is plausibly due to a more complicated slip process associated with fluid injection into a spatial complex permeability structure such as $\kappa(x,y,z) \sim \exp(\alpha\varphi(x,y,z))$ as modelled at lower right in Fig 13.

Consistent blue-trace records and associated spectra of compact P- and S-wave pulses characteristic of fault-like slip processes indicates that seismic motion registered by the grouted-accelerometer array up to 500 Hz frequencies is not significantly distorted by sensor instability. The largely consistent spectral content of the red traces indicates that signal distortion is not a significant factor in the high frequency waveforms to ~1200 Hz. Evidence of high frequency waveform fidelity to 1 kHz allows a coherent interpretation of high frequency seismic radiation in terms of dynamic slip on fluid-pressure induced planar structures local to the hydrofracture wellbore that are embedded in spatially complex crustal volumes such as the crustal permeability structures $\kappa(x,y,z) \sim \exp(\alpha\varphi(x,y,z))$ discussed in §2.1.

Examples of complex seismic emission spectra analogous to the black traces of Fig 12 and red traces of Fig 15 are seen in the acoustic emission (AE) waveform spectra acquired from laboratory rock samples stressed towards failure [87]. Fig 16 rock sample emissions are not due to rock failure on planar surfaces (e.g., Fig 12 red traces, Fig 13 upper left), but are instead generated by seismic slip on localised zones of weakness (e.g., Fig 12 black traces, Fig 13 lower right). At 500kHz rather than 500Hz, the seismic frequencies are three decades higher than the field examples; but the interpretational gap is closed by scaling: 10mm zones rock samples translate into 10m zones in sandstone hydrofractures and ambient basement crust permeability structures.

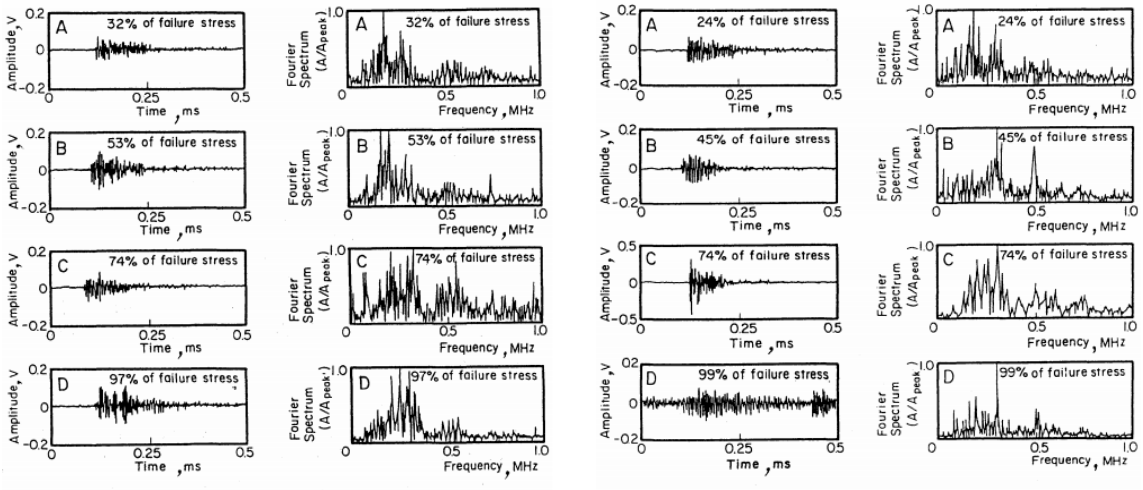

Fig 16 – Waveforms and waveform spectra recorded for laboratory rock failure sequences of granite (left) and sandstone (right). The complex waveform spectra resemble Fig 12 spectra from slip event radiation recorded at 2.5km depth for crystalline basement stimulation at 6km depth, the Fig 13 lower-right synthetic spectra for slow slip on spatially correlated roughness, and Fig 15 high frequency spectra from hydrofractures in sandstones.

We note in passing that the authors of the Fig 16 study find it significant that the left-hand rock sample is granite, a ''heterogeneous'' rock, and the right-hand sample is sandstone, a ''homogeneous'' rock. It puzzles the authors that two rock types have closely similar failure waveforms and waveform spectra. From our point of view, granite and sandstone have the same internal porosity and permeability structures, and therefore should fail in comparable manners (if not necessarily at the same stress levels).

Figs 12-16 show field-scale to lab-scale evidence for seismic waveforms and waveform spectra that do not conform to radiation from crustal dislocation slip on planar fault structures. Whether at 6km depth in crystalline basement, 2.5km depth in tight gas sands, or in the laboratory samples undergoing strain failure, complex high-frequency seismic radiation is emitted during dislocation slip within the rock volume. Modelling seismic waveforms emitted by dynamic dislocation slip in spatially complex zones of weakness due to high-porosity and high permeability reproduces the observed seismic radiation waveform spectral distributions.

The degree of spatial complexity in rock that best reproduces the observed seismic radiation waveform spectra is consistent with the spatially correlated poroperm structures $\kappa(x,y,z) \sim \exp(\alpha\varphi(x,y,z))$, $\alpha \sim 20$, derived from the empirics of spatially-correlated rock-fluid interactions observed throughout the crust. We may plausibly express the close physical relationship between ambient crust microseismic events and crustal permeability sites as ''Meqs ~ Permeability''.

4. DISCUSSION/CONCLUSIONS

Applying the materials and methods of spatially correlated porosity and permeability in the ambient crust gives new perspectives on crustal flow stimulation and flow imaging. Coupling spatially correlated crustal microseismicity to spatially correlated crustal permeability structures contrasts strongly with the historical association of fault-slip seismicity with fault-like fluid conduits in crustal rock. Figs 1-16 present physical and statistical evidence across five to six decades of scale length – from AE failure events in stressed rock samples at cm-scales to 5-km-scale spatial correlations of southern California tectonic province seismicity – that crustal microseismicity is an active ingredient in spatially-correlated crustal fluid flow structures. In contrast, the fault-slip structure of faults applied to ambient crust microseismicity and reservoir planar-flow fluid conduits is constrained by nothing more demanding than the G-R fractal scaling of slip-conduit size-frequency distributions.

On closer examination, it appears that evidence connecting fault-like conduit flow to fault-slip seismicity is essentially a conjecture that is based on the default assumption that what happens at one scale in the crust is wholly representative of what happens at any other scale. This assumption is accurate only for materials in which physical property spatial variations are uncorrelated at all relevant scales. In the case of crustal porosity (as with other fluid-flow-related physical variables such as fracture density, ionic conductivity, radionuclide abundances), uncorrelated spatial fluctuations exist only if well-log Fourier power spectra are flat, i.e., for porosity $S_\varphi(k) \sim 1/k^\beta$, $\beta \sim 0$, over the cm-km scale range. As almost universally observed in the ambient crust, however, porosity (and related physical property) well-log Fourier power spectra scale inversely with spatial wavenumber k, $S_\varphi(k) \sim 1/k^\beta$, $\beta \sim 1$, over the observed five decades of scale length $1/km < k < 1/cm$ [68-69].

Freely interpolating crustal properties between two widely separated scale lengths is a standard procedure in early considerations of geothermal heat extraction. Examples include up-scaling wellbore hydrofracture processes observed at the m-scale to projected behaviour at km scales [88] and up-scaling fluid flow studies on laboratory prepared rock surfaces at the cm-scale to notionally validate laminar flows on m-to-km-scale planar conduits [47]. Reminders of this uncomplicated and unexamined freedom-to-scale assumption are in the two following statements. M-to-km upscaling of fracture mechanics informs a 1971 Los Alamos National Laboratory exploratory report on crustal heat extraction [88]:

> *Water at a pressure of about 100 kg/cm^2 (1500 psi) would then be injected from the surface to form and extend a thin, circular, vertical crack centered at the 4-km depth…..For a crack having a radius of 1 km (3300 ft), the volume is about 5.3 x 10^5 m^3 and the work is 5.3 x 10^{12} joules.*

A parallel cm-to-m-km upscaling of fluid flow in crustal fractures is notionally provided by contemporary Lawrence-Berkeley National Laboratory rock mechanics observations [47]:

> *We visualize the process of a fracture that is closing under normal stress as being controlled by the strength of the asperities that are in contact. These contact areas are able to withstand significant stresses while maintaining space for fluids to continue to flow as the fracture aperture decreases. … Thus one does not see any noticeable shift in correlations of the experimental results in passing from an open fracture to one where the surfaces are being closed under stress.*

In the 50 years since the conjectured geothermal heat extraction via fluid flow in planar fractures generated by high pressure fluid injection into the crust was circulated, little or no confirmatory evidence has emerged to support the conjectured flow process. From a recent paper on crustal permeability attributing to brittle deformation features -- fractures, faults, joints, and veins -- the dominant role for fluid flow in the brittle crust, it is clear that field-scale fracture-borne flow mechanisms remain inferred rather than observed [89]:

> *Permeability….can be retrieved from the transmissivity T [m^2 sec^{-1}] calculated from hydraulic test data. From the experimentally derived transmissivity T, the hydraulic conductivity K [m sec^{-1}] can be computed. Quantifying T and K from pressure-time data obtained in well tests requires geological expertise and ideas about the geological and hydraulic structure of the subsurface. The parameter K is not measured data; it is ultimately the result of a modelling process.*

We interpret the Fig 1-16 perspective on crustal flow mechanisms and their association with crustal microseismicity as providing two fundamental correctives to the long-standing but largely unvalidated view that crustal fluid flow proceeds via fault-like planar slip structures. First, we see fluids as an inherent rather than an incidental part of crustal rock-fluid complex. Second, we see that ambient crust rock-fluid interaction systems are spatially correlated rather than spatially uncorrelated at all relevant scale lengths. The key application of these two correctives is that crustal reservoir fluid flow of interest is characterised by large-scale spatially-erratic long-range-correlated poro-connectivity structures rather than by essentially incidental occurrences of statistically independent planar slip structures through which crustal fluids flow haphazardly with no degree of interaction with the enclosing rock mass. §§3.1-3.4 discuss applied field scale evidence for ‘’Meq ~ Permeability’’.

3.1 Erratic crustal fluid flow structures associated with $\kappa(x,y,z) \sim \exp(\alpha\varphi(x,y,z))$, $\alpha \sim 20$

The role of crustal microseismicity in crustal reservoir characterisation and management shifts emphatically with the spatial-correlation perspective. Apart from reservoir systems in active fault zones, the relation between microseismic slip events and principal reservoir fluid flow structures becomes complexly and subtly structured rather than simply haphazardly unstructured. Key flow structures need not be coincident with large slip events if the given slip surface is not connected to large-scale fluid source and sink flow structures. Instead, the flow structures of account within a reservoir volume can arise from large-scale spatially erratic but diffuse poro-connectivity structures that cannot be statistically recognised or predicted from sparse small-scale sampling. From the new perspective on reservoir microseismicity, the major reservoir flow structures of interest can be, and must be, mapped by detecting and locating flow-connectivity sites of persistent small-scale slip events triggered by ongoing active flow-pressure variations along large-scale poro-connectivity percolation pathways. Fig 17 pictorially summarises the complexly and subtly structured flow pathways inherent in the §2 ambient crust. Such spatial complexity cannot be modelled or discussed coherently by application of the uncorrelated randomness embedded in the standard picture of fault-like fluid flow conduits.

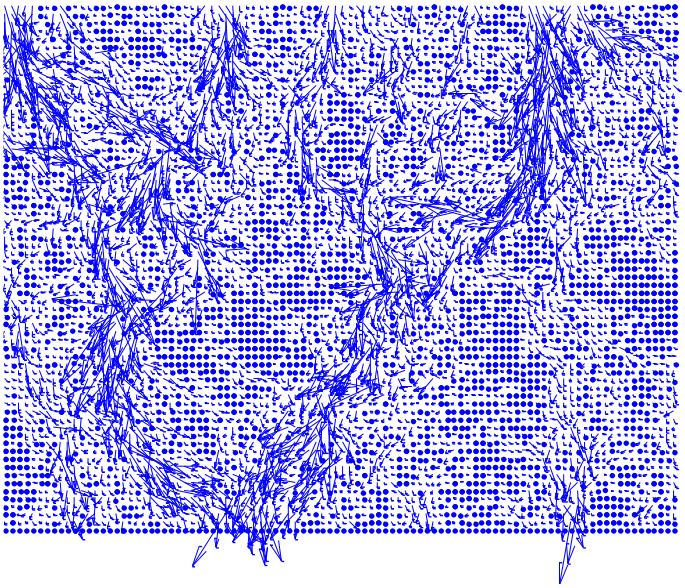

Fig 17 – Illustration of fluid flow spatial complexity in 2d realisation of the $\kappa(x,y,z) \sim \exp(\alpha\varphi(x,y,z))$, $\alpha \sim 20$, permeability structure associated in §2 with ambient crust microseismicity. The areas of active flow denoted by flow vectors emit low level seismic energy as summarised by Meq ~ Permeability. Detecting and tracking such microseismicity emissions is required to effectively manage crustal reservoir fluid resources.

3.2 Induced microseismic slip in spatially correlated poroperm structures

It is wide-spread practice in reservoir modelling to assume that complex rock processes involving many physical variables with unknown values will tend to average out to an ''effectively homogeneous'' medium. A pervasive manifestation of this practice is populating reservoir models with ''fractures'' that provide cubic-law conduits for reservoir fluids [55-56, 58-59]. On the assumption that small-scale variations in rock properties can be ignored through spatial averaging, fracture models are created by random assemblages of fault parameters on the presumption that the details of single fractures are irrelevant to the overall flow properties of the fault assemblage. While these facture constructs enable the performance of thermal depletion histories, their use over a period of 40 years has provided no satisfactory interaction with crustal observation since the introduction exploratory single fracture thermal modelling. In particular, the connection details between flow structures in crustal volumes and the wellbores drilled into the volumes has been largely ignored.

We can look quantitatively at modelling based on uncorrelated randomness. Under the aegis of the central limit theorem, multiple complex physical processes in the crust are assumed to lead to normal distributions for net physical processes such as crustal flow. As normal distributions are strictly bounded in deviation from the norm, it is automatic that spatial variations in the net crustal processes such as flow are conveniently bounded. If there happen to be large scale variations in the modelled crustal structure, the standard modelling step is to partition the crustal structure into sections, with each section characterised by a specific section mean value and its standard deviation. Such composite models are then defined as much by the interfaces between the distinct material sections as by the properties of the material sections themselves.

Several flaws appear in the above modelling scenario applied to crustal flow systems. For the central limit theorem to apply, it is formally required that events within the physical processes must be spatially independent. If event processes are spatially independent then a spatial sequence of process-relevant rock physical variables X_m, m = 0….M, measured by a well-log must have a flat Fourier power spectrum, $S_X(k) \sim 1/k^{\beta}$, $\beta \sim 0$. If crustal sectioning has caused interfaces to appear in the model, then the interfaces contribute their own spectral scaling, $S(k) \sim 1/k^{\beta}$, $\beta \sim 2$.

The problem with this style of crustal modelling is that neither $\beta \sim 0$ nor $\beta \sim 2$ spectral-power scaling property exponents is observed in the crust. Instead, as indicated in foregoing sections, the observed spectral-power scaling exponent attested for crustal well-logs worldwide is $\beta \sim 1$. The intermediate spatial correlation scaling exponent $\beta \sim 1$ is not a statistical artefact of the trade-offs between the two extremes $\beta \sim 0$ and $\beta \sim 2$. Rather, as discussed below, $\beta \sim 1$ is trade-off between complete crustal physical disorder ($\beta \sim 0$) and complete crustal physical order ($\beta \sim 2$) in the rock-fluid interactions that occur at all scale lengths of mm to km [67].

The spatial structures of crustal rock-fluid interactions arising from the physical processes leading to the $\beta \sim 1$ spatial correlation exponent have no natural boundedness as illustrated in Fig 17. Formally speaking, spatial means and deviations from the mean have no physical or statistical validity in treating crustal permeability distributions $\kappa(x,y,z) \sim \exp(\alpha\varphi(x,y,z))$, $\alpha \sim 20$.

The inherent drawback of uncorrelated random fracture modelling is highlighted by the persistent problem of why fault-slip events stop rather than persisting [e.g., 40]. The seismic slip properties of uncorrelated random fracture assemblages provide no conceptual means by which to limit the spatial extent of seismic dislocation slip within the fracture assemblage. As a result, fault-rupture stopping mechanisms for seismic slip in spatially uncorrelated fracture models are inserted by hand to conform with observation. In line with observed fluid injection stimulation of the ambient crust, lognormally distributed crustal permeability populations $\kappa(x,y,z) \sim \exp(\alpha\varphi(x,y,z))$, $\alpha \sim 20$, provide naturally occurring spatial bounds that inherently limit the (probable) extent of spatial slip in the ambient crust. In a properly conceived numerical rock mass, unbounded seismic slip can be seen as naturally highly improbable for physical reasons that are far more robust than statistical reasons [90].

REFERENCES

[1] Richter CF (1935) An instrumental earthquake magnitude scale, Bulletin of the Seismological Society of America, Vol. 25, No. 1.
[2] Gutenberg B & Richter CF (1941) Seismicity of the Earth, Geological Society of America, Special Paper No 34
[3] Gutenberg B & Richter CF (1944) Frequency of earthquakes in California, Bull Seis Soc Amer 34, 185-188.
[4] Gibbs JF, Healy JH, Raleigh CB & Coakley J (1973) Seismicity in the Rangely, Colorado, area: 1962-1970, Bulletin of the Seismological Society of America, Vol. 63, No. 5, 1557-1570.
[5] Aki K (1981) A probabilistic synthesis of precursory phenomena, in Earthquake Prediction: An International Review, Maurice Ewing Set., vol. 4, edited by D. W. Simpson and P. G. Richards, pp. 566-574, AGU.
[6] Shi Y & Bolt BA (1982) The standard error of the magnitude-frequency b value, Bulletin of the Seismological Society of America, Vol. 72, No. 5, pp. 1677-1687.
[7] King G (1983) The accommodation of large strains in the upper lithosphere of the earth and other solids by self-similar fault systems: The geometrical origin of b-value, Pure Appl. Geophys., 121, 761-815.
[8] Scholz, C. H., and C. A. Aviles (1986) The fractal geometry of faults and faulting, in Earthquake Source Mechanics, Geophys. Monogr. Set., vol. 37, edited by S. Das et al., pp. 147-155, AGU.
[9] Okubo PG & Aki K (1987) Fractal geometry in the San Andreas fault system, J. Geophys. Res., 92, 345-355.
[10] Hirata T, Satoh T & Ito K (1987) Fractal structure of spatial distribution of microfracturing in rock, Geophys. J. R. astr. Soc. 90, 369-374.
[11] Hirata T (1989) A correlation between the b value and the fractal dimension of earthquakes, Journal of Geophysical Research, 94, 7507-7514.
[12] Utsu T (1999) Representation and analysis of the earthquake size distribution: A historical review and some new approaches, Pure and Applied Geophysics 155, 509-535.
[13] Haskell NA (1964) Total energy and energy spectral density of elastic wave radiation from propagating faults, Bull Seis Soc Amer 54, 118-142.
[14] Haskell NA (1966] Total energy and energy spectral density of elastic wave radiation from propagating faults, Part 2, Bull Seis Soc Amer 56, 125-140.

[15] Haskell NA (1969) Elastic displacements in the near-field of a propagating fault, Bull Seis Soc Amer 59, 865-908.
[16] Kanamori H (1972) Determination of effective tectonic stress associated with earthquake faulting. The Tottori earthquake of 1943, Phys. Earth Planet. Interiors 5, 426-434.
[17] Trifunac MD (1972) Stress estimates for the San Fernando, California, earthquake of February 9, 1971: Main event and thirteen aftershocks, Bull Seis Soc Amer 62, 721–750.
[18] Brune, J. (1970). Tectonic Stress and Spectra of Seismic Shear Waves from Earthquakes, J. Geophys. Res., 75, 4997 – 5009; Brune, J. N. (1971). Correction: Tectonic stress and the spectra of seismic shear waves from earthquakes, J. Geophys. Res., 76, 5002.
[19] Kanamori H & Anderson DL (1975) Theoretical basis of some empirical relations in seismology, Bull Seis Soc Amer 65, 1073-1095.
[20] Kanamori H (1977) The energy release in great earthquakes, Journal Geophysical Research 82, 2981-2987.
[21] Aki K & Richards P (1980) Quantitative Seismology, 2 Vols, W. H. Freeman, San Francisco, 932 pp.
[22] Madariaga R (2010) Earthquake Scaling Laws. 10.1007/978-1-4419-7695-6_22.
[23] Rutledge JT, Phillips WS & Mayerhofer MJ (2004) Faulting Induced by Forced Fluid Injection and Fluid Flow Forced by Faulting: An Interpretation of Hydraulic-Fracture Microseismicity, Carthage Cotton Valley Gas Field, Texas, Bull Seis Soc Amer 94, 1817–1830
[24] Eisner L, Duncan PM, Heigl WM & Keller WR (2009) Uncertainties in passive seismic monitoring, Leading Edge, vol. 28, no. 6, pp. 648–655.
[25] James P, Verdon J, Kendall JM and Maxwell SC (2010) A comparison of passive seismic monitoring of fracture stimulation from water and CO2 injection, Geophysics 75; doi: 10.1190/1.3377789
[26] Warpinski NR, Du J & Zimmer U (2012) Measurements of hydraulic-fracture-induced seismicity in gas shales, SPE Hydraulic Fracturing Technology Conference, Houston TX; SPE 151597.
[27] Majer E, Nelson J, Robertson-Tait A, Savy J & Wong I (2012) Protocol for Addressing Induced Seismicity Associated with Enhanced Geothermal Systems, DOE/EE-0662.
[28] Douglas J, Edwards B, Convertito V, Sharma N, Tramelli A, Kraaijpoel D, Cabrera BN, Maercklin N & Troise C (2013), Predicting Ground Motion from Induced Earthquakes in Geothermal Areas, Bulletin of the Seismological Society of America, Vol. 103, No. 3, pp. 1875–1897; doi: 10.1785/0120120197.
[29] Edwards B & Douglas J (2014) Magnitude scaling of induced earthquakes, Geothermics 52, 132-139; doi: 10.1016/j.geothermics.2013.09.012.
[30] Kwiatek G, Saarno T, Ader T, Bluemle F, Bohnhoff M, Chendorain M, Dresen G, Heikkinen P, Kukkonen I, Leary P, Leonhardt M, Malin P, Martínez-Garzón P, Passmore K, Passmore P, Valenzuela S & Wollin C (2019) Controlling fluid-induced seismicity during a 6.1-km-deep geothermal stimulation in Finland, Science Advances 01 May 2019: Vol. 5, no. 5, eaav7224 DOI: 10.1126/sciadv.aav7224.
[31] Gibbs JF, Healy JH, Raleigh CB & Coakley J (1972) Earthquakes in the Oil Field at Rangely, Colorado, U.S. Geological Survey Open-File Report, p. 27.
[32] Heimpel M (1996) Earthquake size-frequency relations from an analytical stochastic rupture model, J Geophysical Research: Solid Earth 101(B10), 22435–22448 doi:10.1029/96jb01888.
[33] Wiemer S & Wyss M (2000) Minimum magnitude of completeness in earthquake catalogs: Examples from Alaska, the western United States, and Japan. Bull Seismol Soc Am. 90: 859-869.
[34] Woessner J & Wiemer S (2005) Assessing the quality of earthquake catalogues: Estimating the magnitude of completeness and its uncertainty. Bull Seismol Soc Am. 95: 684-698. DOI:10.1785/0120040007
[35] Shapiro S, Dinske C, Langenbruch C & Wenzel F (2010). Seismogenic index and magnitude probability of earthquakes induced during reservoir fluid stimulations. The Leading Edge. 29. 304-309. 10.1190/1.3353727.
[36] Bachmann CE, Wiemer S, Goertz-Allmann BP & Woessner J (2012) Influence of pore-pressure on the event-size distribution of induced earthquakes, Geophysical Research Letters 39, L09302; doi:10.1029/2012GL051480.
[37] Mignan A (2012) Functional shape of the earthquake frequency-magnitude distribution and completeness magnitude, Journal of Geophysical Research 117, doi:10.1029/2012JB009347
[38] Mignan A. & Woessner J (2012). Estimating the magnitude of completeness for earthquake catalogs. Community Online Resource for Statistical Seismicity Analysis. 10.5078/corssa-00180805.
[39] Zaky DA, Nugraha AD, Sule R, & Jousset P (2015) Spatial analysis of earthquake frequency-magnitude distribution at geothermal region in the south of Bandung, West Java, Indonesia, 9th International Workshop on Statistical Seismology, 14 - 18 June, Potsdam, Germany.
[40] Galis M, Ampuero JP, Mai PM & Cappa F (2017) Induced seismicity provides insight into why earthquake ruptures stop. Sci. Adv. 3, doi:10.1126/sciadv.aap7528.
[41] Zhou Y, Zhou S & Zhuang J (2018) A test on methods for MC estimation based on earthquake catalog, Earth and Planetary Physics 2: 150–162; doi: 10.26464/epp2018015.
[42] Warren JE, Price HS. Flow in heterogeneous porous media. Soc Pet Eng J. 1961; 1: 153-169.
[43] Warren JE, Skiba FF. Macroscopic dispersion. Soc Pet Eng J. 1964; 4: 215-230.
[44] Warren JE & Root PJ (1963) The behavior of naturally fractured reservoirs, Society of Petroleum Engineers Journal, 245–255.
[45] Gringarten AC, Witherspoon PA & Ohnishi Y (1975) Theory of heat extraction from fractured hot dry rock, Journal of Geophysical Research, 1120-1124.
[46] Wunder R & Murphy H (1978) Singly and multiply fractured hot dry rock reservoirs, Los Alamos National Laboratory Report, LA7219-MS, UC-66a, 1-15.
[47] Witherspoon PA, Wang JY, Iwai K & Gale JE (1980) Validity of Cubic Law for Fluid Flow in a Deformable Rock Fracture, Water Resources Research 16, 1016-1024.
[48] Arbogast T, Douglas, Jr. J & Hornung U (1990) Derivation of the double porosity model of single phase flow via homogenization theory, Siam J. Math. Anal. Vol. 21, No. 4, Pp. 823–836.
[49] Zimmerman RW & Bodvarsson G (1994) Hydraulic conductivity in rock fractures, LBL-35976 UC-800.
[50] Sisavath S, Al-Yaarubi A, Pain CC & Zimmerman RW (2003) A simple model for deviations from the cubic law for a fracture undergoing dilation or closure. PAGEOPH 160, 1009–1022.

[51] Tester JW et al (2006) The Future of Geothermal Energy, Impact of Enhanced Geothermal Systems (EGS) on the United States in the 21st Century, http://geothermal.inel.gov.
[52] Sutter D, Fox DB, Anderson BJ, Koch DL, von Rohr PR & Tester JW (2011) Sustainable heat farming of geothermal systems: a case study of heat extraction and thermal recovery in a model EGS fractured reservoir, Proceedings 36th Workshop on Geothermal Reservoir Engineering, Stanford University, 31 January–2 February 2011.
[53] Zimmerman RW (2012) The history and role of the cubic law for fluid flow in fractured rocks. In Proceedings of the Session H071 Dynamics of Fluids and Transport in Fractured Porous Media, San Francisco.
[54] Pruess K, Oldenburg C & Moridis (2012) TOUGH2 User's Guide, Version 2.1, Tech. Rep. LBNL-43134, Lawrence Berkeley National Laboratory; Pruess K (2003) The TOUGH Codes - A Family of Simulation Tools for Multiphase Flow and Transport Processes in Permeable Media MS 90-1 1 16, LBNL.
[55] FracMan: Doe T, McLaren R, & Dershowitz W (2014) Discrete Fracture Network Simulations of Enhanced Geothermal Systems, 39th Workshop on Geothermal Reservoir Engineering Stanford University, February 24-26, SGP-TR-202.
[56] Elmo D, Rogers S, Stead D & Eberhardt E (2014) Discrete Fracture Network approach to characterise rock mass fragmentation and implications for geomechanical upscaling, Journal Mining Technology, Transactions of the Institutions of Mining and Metallurgy, Vol 123; doi.org/10.1179/1743286314Y.0000000064.
[57] Jain C, Vogt C & Clauser C (2015) Maximum potential for geothermal power in Germany based on engineered geothermal systems, Geothermal Energy (2015); DOI 10.1186/s40517-015-0033-5.
[58] Lei Q, Latham J-P & Tsang C-F (2017) The use of discrete fracture networks for modelling coupled geomechanical and hydrological behaviour of fractured rocks, Computers and Geotechnics 85 (2017); http://dx.doi.org/10.1016/j.compgeo.2016.12.024;
[59] Alghalandis YF, Elmo D & Eberhardt E (2017) Similarity Analysis of Discrete Fracture Networks, arXiv:1711.05257.
[60] Leary P, Malin P, Saunders G & Sicking C (2020) Seismic Imaging of Convective Geothermal Flow Systems to Increase Well Productivity, Journal of Energy and Power Technology 2(3); doi:10.21926/jept.2003012.
[61] Leary P & Malin P (2020) Correlation function $\Gamma_{meq}(r) \sim 1/r^{1/2}$ coupling of microseismicity to permeability -- The basis for fluid flow seismic image targeting for geothermal production wells, Proceedings World Geothermal Congress 2021 Reykjavik, Iceland, 21-26 May 2021.
[62] Leary P, Malin P, Saarno T, Heikkinen P, Diningrat W (2019) Coupling crustal seismicity to crustal permeability - Power-law spatial correlation for EGS-induced and hydrothermal seismicity. Proceedings of the 44th Workshop on Geothermal Reservoir Engineering, Stanford University, February 11-13.
[63] Leary P, Malin P, Pogacnik J, Rugis J, Valles B & Geiser P (2014) Lognormality, dk ~ kdf, EGS, and all that, Proceedings 39th Stanford Geothermal Workshop, February 24-26 2014, Stanford University, CA.
[64] Malin P, Leary P, Shalev E, Rugis J, Valles B, Boese C, Andrews J & Geiser P (2015) Flow Lognormality and Spatial Correlation in Crustal Reservoirs: II – Where-to-Drill Guidance via Acoustic/Seismic Imaging, WGC2015, 19-24 April, Melbourne AU
[65] Leary P, Malin P & Niemi R (2017) Finite-Element Modelling of Wellbore-Observed Fracture-Borne Heat Advection – Application to EGS Stimulation in Basement Rock, 41st Workshop Geothermal Reservoir Engineering, Stanford University, February 13-15, SGP-TR-212;
[66] Leary P, Malin P & Niemi R (2017) Fluid flow & heat transport computation for power-law scaling poroperm media, Geofluids, Volume 2017, https://doi.org/10.1155/2017/9687325
[67] Leary P, Malin P, Saarno T, Kukkonen I (2018) $\alpha\varphi \sim \alpha\varphi_{crit}$ - Basement rock EGS as extension of reservoir rock flow processes. Proceedings 43th Workshop on Geothermal Reservoir Engineering, Stanford University, 2018 February 12-14.
[68] Leary PC (1997) Rock as a critical-point system and the inherent implausibility of reliable earthquake prediction. Geophys J Int. 131: 451-466.
[69] Leary PC (2002) Fractures and physical heterogeneity in crustal rock, in Heterogeneity in the Crust and Upper Mantle: Nature, Scaling, and Seismic Properties, J. A. Goff and K. Holliger, Eds., pp. 155–186, Kluwer Academic/Plenum Publishers, New York, NY, USA, 2002.
[70] Leary P, Malin P, Saarno T & Kukkonen I (2017) Prospects for Assessing Enhanced Geothermal System (EGS) Basement Rock Flow Stimulation by Wellbore Temperature Data, Energies, vol 10, no. 12, DOI: 10.3390/en10121979.
[71] Leary P, Malin P & T Saarno (2020) A Physical Basis for the Gutenberg-Richter Fractal Scaling, 45th Workshop on Geothermal Reservoir Engineering, Stanford University, February 10-12, SGP-TR-216 1.
[72] *Totsuji H & Kihara T* (1969) The correlation function for the distribution of galaxies, *Publications* of the Astronomical *Society* of *Japan*, vol. *21*, p.*221*.
[73] Fall SM (1979) Correlations in the distribution of galaxies provide some important clues about the structure and evolution of the Universe on scales larger than individual galaxies, Reviews of Modern Physics 51, 21-43 DOI: 10.1103/RevModPhys.51.21.
[74] Landau LD & Lifshitz EM (1980) *Statistical Physics*, Pergamon Press, Oxford.
[75] Kagan YY & Knopoff L (1980) Spatial distribution of earthquakes: the two-point correlation function, *Geophysical Journal Royal Astronomical Society* 62, 303-320.
[76] Hillers G, Mai PM, Ben-Zion Y & Ampuero JP (2007) Statistical properties of seismicity of fault zones at different evolutionary stages, Geophys. J. Int. (2007) 169, 515–533 doi: 10.1111/j.1365-246X.2006.03275.x
[77] Kagan YY (2007) Seismology Earthquake spatial distribution: The correlation dimension, Geophys. J. Int. 168, 1175–1194; doi: 10.1111/j.1365-246X.2006.03251.x
[78] Mouslopoulou, V., and D. T. Hristopulos (2011) Patterns of tectonic fault interactions captured through geostatistical analysis of microearthquakes, J. Geophys. Res., 116, B07305, doi:10.1029/2010JB007804.
[79] Verdon J (2013) Fractal Dimension of Microseismic Events via the Two-Point Correlation Dimension, and its Correlation with b Values. 4th EAGE Passive Seismic Workshop. 10.3997/2214-4609.20142359.
[80] Mohammad Javad Afshari Moein Thessa Tormann Benoît Valley Stefan Wiemer (2018) Maximum Magnitude Forecast in Hydraulic Stimulation Based on Clustering and Size Distribution of Early Microseismicity, Geophysical Research Letters, https://doi.org/10.1029/2018GL077609
[81] Leary P & Malin P (2020) MEQ ~ Permeability – Modelling High Frequency Emissions from Stimulation-Induced Seismic Activity in the Ambient Crust, Proceedings World Geothermal Congress 2021 Reykjavik, Iceland, 21-26 May 2021.

[82] Peter Leary, Peter Malin, Tero Saarno & Pekka Heikkinen (2020) St1 Deep Heat EGS Project -- Computation of wellbore-to-wellbore permeability stimulation, Proceedings World Geothermal Congress, Reykjavik, Iceland, 21-26 May 2021
[83] Abercrombie RE (1996) The magnitude-frequency distribution of earthquakes recorded. with deep seismometers at Cajon Pass, southern California, Tectonophysics 261, 1-7.
[84] Branagan PT, Warpinski NR, Peterson RE, Hill RE & Wolhart SL (1997) Propagation of a Hydraulic Fracture into a Remote Observation Wellbore: Results of C-Sand Experimentation at the GRI/DOE M-Site Project, SPE38574.
[85] Nolen-Hoeksema RC & Ruff LJ (2001) Moment tensor inversion of microseisms from the B-sand propped hydrodracture, M-site, Colorado, Tectonophysics 336, 163-181.
[86] Lorenz JC (2012) "MWX -The Multiwell Experiment in the Piceance Basin, Colorado: Reprise from 30 Years Ago," AAPG Search and Discovery, Article ID 70129.
[87] Michihiro K, Kata K, Fujiwara T & Yoshioka H (1997) Prediction of failure in rock masses by acoustic emission, Materials Science Research International, Vol.3, No.2 pp. 106-111.
[88] Robinson ES, Potter RM, Mclnteer EB, Rowley JC, Armstrong DF & Mills RF (1971) A Preliminary Study of the Nuclear Subterrene, LA-4547 UC-38 April 1971.
[89] Stober I & Bucher K (2015) Hydraulic conductivity of fractured upper crust: insights from hydraulic tests in boreholes and fluid-rock interaction in crystalline basement rocks, Geofluids 15, 161–178 doi: 10.1111/gfl.12104
[90] Trutnevyte E & Azevedo IL (2018) Induced seismicity hazard and risk by enhanced geothermal systems: an expert elicitation approach, Environ. Res. Lett. 13 (2018) 034004 https://doi.org/10.1088/1748-9326/aa9eb2
[91] Brehme M, Regenspurg S, Leary P, Bulut F, Milsch H, Petrauskas S, Valickas R & Blöcher G (2018) Injection-triggered occlusion of flow pathways in geothermal operations, Geofluids, Vol 2018, Article ID 4694829; https://doi.org/10.1155/2018/4694829.
[92] Brehme M & Leary P (2020) Understanding geothermal return well injectivity decline -- The case for spatially correlation poroperm distributions rather than deep-bed filtration Proceedings World Geothermal Congress 2020 Reykjavik, Iceland, 21-26 May 2021
[93] Leary P & Malin P (2016) Simple Analytics for EGS: Quantifying Wellbore-centric Crustal Heat Extraction by Peclet Parameters 41st Workshop on Geothermal Reservoir Engineering Stanford University, February 22-24, SGP-TR-209 1